

# Is there a tilt in the fundamental (hyper)plane?★

M. D’Addona<sup>1,2,3</sup>, A. Mercurio<sup>1,2,4</sup>, C. Grillo<sup>5,6</sup>, P. Rosati<sup>3,7</sup>, G. Granata<sup>3,5,8</sup>, G. Angora<sup>2,3</sup>,  
M. Annunziatella<sup>9</sup>, P. Bergamini<sup>5,7</sup>, V. Bozza<sup>1,2,4</sup>, G. B. Caminha<sup>10</sup>, A. Gargiulo<sup>6</sup>, F. Getman<sup>2</sup>,  
M. Girardi<sup>11,12</sup>, A. Grado<sup>2</sup>, L. Limatola<sup>2</sup>, M. Lombardi<sup>5,7</sup>, M. Meneghetti<sup>7</sup>, L. Pecoraro<sup>1,2</sup>, R. Ragusa<sup>2</sup>, L.  
Tortorelli<sup>13,14</sup>, and E. Vanzella<sup>7</sup>

<sup>1</sup> Università di Salerno, Dipartimento di Fisica "E.R. Caianiello", Via Giovanni Paolo II 132, I-84084 Fisciano (SA), Italy

<sup>2</sup> INAF – Osservatorio Astronomico di Capodimonte, Via Moiariello 16, I-80131 Napoli, Italy

<sup>3</sup> Dipartimento di Fisica e Scienze della Terra, Università degli Studi di Ferrara, via Saragat 1, I-44122 Ferrara, Italy

<sup>4</sup> INFN – Gruppo Collegato di Salerno - Sezione di Napoli, Dipartimento di Fisica "E.R. Caianiello", Università di Salerno, via Giovanni Paolo II, 132 - I-84084 Fisciano (SA), Italy.

<sup>5</sup> Dipartimento di Fisica, Università degli Studi di Milano, via Celoria 16, I-20133 Milano, Italy

<sup>6</sup> INAF – IASF Milano, via A. Corti 12, I-20133 Milano, Italy

<sup>7</sup> INAF – OAS, Osservatorio di Astrofisica e Scienza dello Spazio di Bologna, via Gobetti 93/3, I-40129 Bologna, Italy

<sup>8</sup> Institute of Cosmology and Gravitation, University of Portsmouth, Burnaby Rd, Portsmouth PO1 3FX, UK

<sup>9</sup> Centro de Astrobiología (CAB), CSIC-INTA, Ctra. de Ajalvir km 4, Torrejón de Ardoz 28850, Madrid, Spain

<sup>10</sup> Max-Planck-Institut für Astrophysik, Karl-Schwarzschild-Str. 1, D-85748 Garching, Germany

<sup>11</sup> Università degli Studi di Trieste, Dipartimento di Fisica - Sezione di Astronomia, via Tiepolo 11, I-34143 Trieste, Italy

<sup>12</sup> INAF – Osservatorio Astronomico di Trieste, via G. B. Tiepolo 11, I-34143, Trieste, Italy

<sup>13</sup> Faculty of Physics, University Observatory, Ludwig-Maximilians-Universität München, Munich, Germany

<sup>14</sup> Institute for Particle Physics and Astrophysics, ETH Zürich, Zürich, Switzerland

Received –; accepted –

## ABSTRACT

**Aims.** We investigate the fundamental plane (FP) of selected early-type (ETG) member galaxies of the galaxy cluster PLCK G287.0+32.9 ( $z_c = 0.3833$ ), exploring also four-dimensional hyperplane extensions.

**Methods.** We measure ETGs structural parameters and photometry from Hubble Space Telescope (HST) observations. We use high-quality spectroscopic data from the Multi Unit Spectroscopic Explorer (MUSE) to measure the galaxy central stellar velocity dispersions and stellar population properties. With this data, we construct the FP trough a robust fitting procedure and analyze its tilt and scatter. We then introduce two hyperplane extensions, one including the stellar mass ( $M^*$ -HP) and another including the stellar over total mass fraction ( $f_e^*$ -HP), and compare their coefficients and scatter to those of the FP.

**Results.** The FP of PLCK G287.0+32.9 is found to have best-fit parameter values consistent with those in the literature ( $\alpha = 1.2 \pm 0.1$  and  $\beta = -0.75 \pm 0.05$ ), with a scatter of 0.09 dex. The ( $f_e^*$ -HP) shows no tilt compared to the theoretical plane ( $\alpha = 2.1 \pm 0.2$  and  $\beta = -1.12 \pm 0.07$ ), with a scatter of 0.042 dex, and the ( $M^*$ -HP) reveals an even tighter relation, with a scatter of only 0.023.

**Conclusions.** Our findings support the idea that the FP is a lower-dimensional projection of a more complex hyperplane and confirm that the variations in the dark matter content contribute significantly to the tilt of the FP. Future studies incorporating larger samples of galaxies and additional physical parameters may further refine our understanding of the FP and its higher-dimensional extensions.

**Key words.** galaxies: clusters: general – galaxies: clusters: individual: PLCK G287.0+32.9 – galaxies: fundamental parameters

## 1. Introduction

Early-type galaxies (ETGs) follow scaling relations that connect their photometric and kinematic properties (e.g. Faber & Jackson 1976; Kormendy 1977a,b,c, 1985). Among them there is the fundamental plane (FP, Eq. 1), which is an observational tight correlation among the logarithms of three physical properties of these galaxies, namely, the effective radius  $R_e$  (i.e. the projected radius of the circle that encloses half of the total light), the average surface brightness  $I_e$  within a circle of radius  $R_e$ , and the value of the stellar velocity dispersion  $\sigma_{e8}$  within a circle of radius  $R_e/8$ . (Djorgovski & Davis 1987; Dressler et al. 1987):

$$\log(R_e) = \alpha \log(\sigma_{e8}) + \beta \log(I_e) + \gamma. \quad (1)$$

This relation is widely used in various contexts, like strong lensing modeling (e.g. Grillo et al. 2015; Monna et al. 2015; Birrer et al. 2020; Granata et al. 2022), and its coefficients can be theoretically derived from a set of assumptions, one of which is that virial theorem holds, so the dynamical mass of a galaxy within  $R_e$  is  $M_e \propto k_{vir} R_e \sigma^2$ , where  $\sigma$  is the central stellar velocity dispersion. Since the average luminosity within  $R_e$  is, by definition,  $L_e = L/2 = \pi R_e^2 I_e$ , and assuming that  $\sigma_{e8} \approx \sigma$ , the total mass-to-light ratio ( $M/L$ ) can be expressed as Eq. (2):

★ Table A.1 is only available in electronic form at the CDS via anonymous ftp to [cdsarc.u-strasbg.fr](http://cdsarc.u-strasbg.fr) (130.79.128.5) or via <http://cdsweb.u-strasbg.fr/cgi-bin/qcat?J/A+A/>

$$\frac{M_e}{L_e} \propto k_{\text{vir}} \frac{\sigma_{e8}^2}{R_e I_e} \implies R_e \propto k_{\text{vir}} \frac{L_e}{M_e^*} \frac{M_e^*}{M_e} \sigma_{e8}^2 I_e^{-1}, \quad (2)$$

where  $M_e^* = M^*/2$  is the stellar mass within the projected stellar half-mass radius  $R_e^*$ . Since the stellar mass distribution is strictly linked to that of the light, one can assume that  $R_e^* = R_e$ . In this case, for a homologous sample of galaxies that have the same stellar mass-to-light ratio ( $M^*/L$ ) and stellar over total mass fraction, within a circle of radius  $R_e$ ,  $f_e^* = M_e^*/M_e$ , the Eq. (2) reduces to Eq. (1) with  $\alpha = 2$  and  $\beta = -1$  (Faber 1987). However, observations show that the FP is tilted with respect to the virial plane, with coefficients varying in the range  $\alpha \in [0.7, 1.5]$  and  $\beta \in [-0.9, -0.6]$ , and it presents an observed scatter of  $\Delta \sim 0.1$  dex (see for example, Bender et al. 1992; Saglia et al. 1993; Jørgensen et al. 1996; Pahre et al. 1998; Bernardi et al. 2003; Jørgensen et al. 2006; van de Sande et al. 2014).

The origin of the tilt and scatter of the FP has been debated for a long time and several studies have shown how different factors can contribute to it, such as the presence of rotational motions (Prugniel et al. 1994; Busarello et al. 1997; Weiner et al. 2006), the stellar mass range and star formation rate (D’Onofrio et al. 2017; Khanday et al. 2022; Grèbol-Tomás et al. 2023; D’Onofrio & Chiosi 2024), the presence of minor and major merging events in the galaxy formation histories (Fernández Lorenzo et al. 2011; Yoon & Park 2020, 2022; Marsden et al. 2022; Kluge & Bender 2023), the dark matter content (Ferrero et al. 2021; de Graaff et al. 2022), and the feedback of active galactic nuclei (AGN) that affect stellar surface density and the  $M/L$  (Rosito et al. 2021). Moreover, non-homology caused by a non-constant stellar initial mass function (IMF), and the presence of  $M^*/L$  gradients tend to reduce  $R_e^*$ , therefore leading to an overestimation of  $M_e^*$  and ultimately causing variations in the estimated total  $M/L$  (Bernardi et al. 2018, 2022, 2023; D’Eugenio et al. 2021).

In the past, the three main causes of the tilt and scatter were thought to be the non-homology, a non constant  $M^*/L$ , and a varying  $f_e^*$ . There is now a broad consensus that  $M/L$  variations contribute significantly to the tilt of the FP, while variations in the stellar populations seem to account for a large fraction of the scatter. For example, Cappellari et al. (2007) analyzed a sample of 25 ETGs at redshift  $z \leq 0.01$  from the Spectroscopic Areal Unit for Research on Optical Nebulae survey (SAURON, Bacon et al. 2001) and showed how  $M/L$  variations could account for up to 90% of the tilt of the FP. This observation was also confirmed by Cappellari et al. (2013) who obtained a very tight relation ( $\Delta \sim 0.07$  dex) in the mass plane (MP) constructed by replacing  $I_e$  with the total mass within  $R_e$  estimated using a dynamic analysis of 260 ETGs from the ATLAS<sup>3D</sup> ( $z \leq 0.01$ , Cappellari et al. 2011). Subsequent studies that used the MP on larger samples of galaxies, such as Li et al. (2018) and Zhu et al. (2024), who used 2000 and 6000 galaxies from the Mapping Nearby Galaxies at the APO survey (MaNGA, Bundy et al. 2015; Westfall et al. 2019), respectively, also found similar results. Hyde & Bernardi (2009a,b) and de Graaff et al. (2021), using a sample of 50000 ETGs from the Sloan Digital Sky Survey (Kollmeier et al. 2019, SDSS) and 1419 ETGs from the Large Early Galaxy Astrophysics Census (LEGA-C, van der Wel et al. 2016; Straatman et al. 2018, up to  $z \sim 0.8$ ) survey, respectively, showed how the observed tilt and scatter of the FP reduce significantly when variations of  $M/L$  ratio are taken into

account by replacing  $I_e$  with the stellar surface mass density  $I_e^* = I_e \cdot M^*/L$ , leaving non-homology and variations in the dark matter content as reasons for the remaining tilt. Similar results were found also by Bezanson et al. (2013) using a sample of 16598 ETGs from the SDSS. Finally, Bernardi et al. (2020) further improved these results by replacing  $R_e$  with  $R_e/k_n$ , where  $k_n$  depends on the shape of the mass profile (or, equivalently, on the Sersic index  $n$ ), and by extending the plane with the axis ratio as a fourth dimension. The relation they obtained presents coefficient values of  $\alpha = 1.904 \pm 0.033$  and  $\beta = -0.776 \pm 0.019$ , that are much closer to the ones of the virial theorem, and it shows a scatter of only  $\Delta \sim 0.05$  dex.

Attempts have been also made to extend the FP to higher dimensional hyperplanes (HP). For example, Gargiulo et al. (2009) were among the first ones to extend the FP with stellar population parameters (such as the metallicity, age, and  $\alpha$ -element abundance ratio  $\alpha/\text{Fe}$ ) using a sample of 141 ETGs from the Shapley Optical Survey ( $z \sim 0.049$ , Mercurio et al. 2006). They found a strong correlation between the scatter and both the age and the  $\alpha/\text{Fe}$  achieving a decrease in the intrinsic scatter to a value as low as  $\Delta = 0.049$  dex. Dogruel et al. (2023, 2024), using 2496 galaxies at  $z < 0.12$  from GAMA, constructed a mass-hyperplane by adding  $\log(n)$  and the  $g - i$  color to Eq. (1) to track the dependence on the morphology and the  $M^*/L$  ratio. However, even though they found that this hyperplane has a lower scatter than the original FP and is not specific to a certain class of galaxies, the coefficients measured for passive galaxies,  $\alpha = 1.071 \pm 0.011$  and  $\beta = -0.627 \pm 0.003$ , are still not compatible with those predicted by the virial theorem. Similar results were also found by D’Eugenio et al. (2024) who built three 4D hyperplanes using either the mass-weighted age, the  $M^*/L$  ratio, or their empirical  $I_{\text{age}}$  as the fourth dimension, exploiting a sample of  $\sim 700$  galaxies with  $z < 0.1$  from Sydney-AAO Multi-object Integral (SAMI, Croom et al. 2012).

In this scientific framework, we exploited Hubble Space Telescope (HST) observations and high-quality spectroscopic data derived from observations made with the Multi Unit Spectroscopic Explorer (MUSE), described in D’Addona et al. (2024, hereafter D24), to build the FP of the members of the galaxy cluster PLCK G287.0+32.9 (PLCK-G287 hereafter), a massive post-merger system at redshift  $z_c = 0.3833$  (Bagchi et al. 2011; Gruen et al. 2014; Bonafede et al. 2014; Zitrin et al. 2017; Finner et al. 2017). We also constructed two 4D hyperplane extensions of the classic FP using stellar masses derived from stellar population analysis.

This paper is structured as follows: in Sec. 2, we describe the spectroscopic and photometric data we used and, in Sec. 3, we outline their analysis. In Sec. 4, we illustrate the construction of the FP of PLCK-G287 and its hyperplane extensions. Finally, in Sec. 5, we discuss the obtained results. Throughout this work, we assume a  $\Lambda$ -CDM cosmology with  $\Omega_{m0} = 0.3$ ,  $\Omega_{\Lambda0} = 0.7$ , and  $H_0 = 70 \text{ km s}^{-1} \text{ Mpc}^{-1}$ , for which  $1'' \approx 5.23 \text{ kpc}$  at the redshift of the cluster PLCK-G287.

## 2. Data

We used the same photometric and spectroscopic data presented in D24, which we summarize here for the sake of clarity.

### 2.1. Photometric data

PLCK-G287 was observed by the HST in the framework of the Reionization Lensing Cluster Survey (RELICS) survey (P.I.: Dan Coe, [Coe et al. 2019](#), program ID 14096) using both the Advanced Camera for Surveys (ACS) and the Wide Field Camera 3 (WFC3). Previous observations made with HST in cycle 23 (P.I.: Seitz, program ID 14165, [Seitz 2016](#)) were also integrated into the RELICS data, for a total of three orbits for the ACS filter group and two orbits for the WFC3 one. We used publicly available images in the two resolutions of  $0.03''$  (30 mas) and  $0.06''$  (60 mas) per pixel. They cover an area, centered on the brightest cluster galaxy (BCG), with a radius of  $\sim 1.7'$  in the optical bands F435W, F475W, F606W, and F814W, and of  $\sim 1.0'$  in the infrared (IR) bands F105W, F110W, F125W, F140W, and F160W. For the first group of filters, the total exposure time varies from a minimum of 2125 s for the F435W band to a maximum of 4680 s for the F814W band, while for the second group it ranges from a minimum of 711 s for the F125W band to a maximum of 11447 s for the F110W band. We ran Sextractor ([Bertini 1996](#)) in dual-image mode on the 60 mas images, using the F814W image as the detection image, and extracted the Kron magnitudes for all available photometric bands.

### 2.2. Spectroscopic data

We used spectroscopic redshift from the catalog published in [D24](#). The redshifts were measured on data acquired with MUSE and the Adaptive Optics Facility (AOF) working in wide field mode ([Ströbele et al. 2012](#); [Arsenault et al. 2008](#)) on three nights in 2019 March-May (P.I.: Amata Mercurio, ESO program 0102.A-0640(A)). We processed and merged the three datacubes produced by these observations following the prescriptions by [Caminha et al. \(2019\)](#), using the reduction pipeline version 2.8.3 ([Weilbacher et al. 2020](#)). The final data cube has an exposure time on target of 3.1 hours in two pointings and 3.8 hours in the westernmost pointing. It covers the center of the galaxy cluster for a total area of  $\sim 3 \text{ arcmin}^2$ , with a spatial resolution of  $0.2''$ , and with a spectral resolution of  $1.25 \text{ Å pixel}^{-1}$  in the vacuum wavelength range from 4700 Å to 9350 Å, with a gap between 5805 Å and 5967 Å due to the emission generated by the guiding laser of the AOF.

## 3. Data analysis

We considered only the spectroscopic members, that were defined in [D24](#) using the redshift range  $0.360 \leq z \leq 0.405$ . Since the relations that define the FP are only valid for virialized ETGs, we selected a sample of passive ETG candidates by selecting the members that are not contaminated by other very close bright galaxies or image artifacts (like star diffraction spikes), and the spectra of which did not present any emission line. We then fitted their light in the 30 mas HST F814W image with Morphofit<sup>1</sup> ([Tortorelli & Mercurio 2023](#); [Tortorelli et al. 2023](#)), using a single Sérsic component model, convolved with the point spread function, and measured their morphological structural parameters from the best fits. We checked the goodness of the fits by inspecting the 2D residual images and the distribution of the residuals and removed from the sample the

<sup>1</sup> Morphofit: a Python package, based on Galfit ([Peng et al. 2002, 2010](#)) and SExtractor ([Bertini 1996](#)), for the morphological analysis of galaxies. See <https://github.com/torluca/morphofit>

galaxies that showed evident spiral arms or substructures that could indicate recent merging events or tidal interactions with faint neighbors. For each of the remaining galaxies in the ETG sample, we re-extracted the 1D spectrum with Specex<sup>2</sup> using a circular aperture with a diameter of  $1.6''$  and spatially weighting the extraction with its best-fit light model. This has been shown to minimize the effect of possible contamination and maximize the spectrum signal-to-noise ratio (S/N; see for example [Granata et al. 2022](#)), while allowing for line-of-sight stellar velocity dispersion (LOSVD) estimates that are on average equivalent to those within the galaxy effective radius ([Granata et al.](#), in preparation). From the spectra, we then measured the LOSVD and the spectrum S/N using pPXF<sup>3</sup> ([Cappellari 2023, 2017](#); [Cappellari & Emsellem 2004](#)). We built our final sample following the criteria introduced by [Tortorelli et al. \(2018\)](#) and [Bergamini et al. \(2019\)](#) and selected a total of 35 ETGs with a spectrum S/N  $\geq 10$ , LOSVD  $\geq 80 \text{ km s}^{-1}$ , and  $n \geq 2.5$  (See Fig. B.1).

Finally, we exploited the software Bagpipes<sup>4</sup> ([Carnall et al. 2018, 2019b](#)) to simultaneously fit the HST multiband photometry and the spectrum of each ETG, and infer their star formation histories (SFH) and physical parameters, such as the total stellar mass  $M^*$ . Bagpipes uses a [Kroupa & Boily \(2002\)](#) initial mass function (IMF) and it is a fixed parameter, so it cannot be changed. We modeled the SFH as a delayed exponentially-decaying function ([Carnall et al. 2019a](#)), that has a star formation rate (SFR) described by Eq. (3).

$$\text{SFR}_{\text{del}}(t) \propto \begin{cases} (t - T_0) \exp\left(-\frac{t-T_0}{\tau}\right) & \text{if } t > T_0 \\ 0 & \text{if } t < T_0 \end{cases} \quad (3)$$

We imposed uniform priors on both the time  $T_0$  since the star formation began and the declining time scale  $\tau$ , allowing them to vary in the range from 0.1 to 15 Gyr and from 0.01 to 10 Gyr, respectively. We also assumed uniform priors on the metallicity  $Z$  in the range 0 to 2.5. We modeled the dust absorption with a Calzetti law ([Calzetti et al. 2000](#); [Calzetti 2001](#)) allowing the attenuation parameter  $A_V$  to vary uniformly from 0 to 8 mag. To reduce the number of free parameters, we fixed the redshift and the stellar velocity dispersion values to the ones we measured from the spectra. The values of the parameters we measured for the 35 ETGs are reported in table A.1.

## 4. The fundamental (hyper)plane of PLCK-G287

From the galfit effective semi-major axis  $a_e^{(\text{gal})5}$  and axis ratio  $q$ , we computed the circularized effective radius  $R_e = a_e^{(\text{gal})} \sqrt{q}$ . We then computed the mean surface brightness  $\mu_e$  by dividing

<sup>2</sup> python-specex: a Python package that provides a set of functions and scripts to handle spectral data-cubes, see: <https://github.com/mauritiusedd/python-specex>.

<sup>3</sup> pPXF: python package that implements a penalized PiXel-Fitting method (pPXF), to extract the stellar or gas kinematics and stellar population from absorption-line spectra of galaxies. See: <https://www-astro.physics.ox.ac.uk/~cappellari/software/>

<sup>4</sup> Bagpipes: a Python package to build complex model galaxy spectra and fit them to arbitrary combinations of spectroscopic and photometric data through the MultiNest nested sampling algorithm ([Feroz & Hobson 2008](#); [Feroz et al. 2009, 2019](#)). See: <https://github.com/ACCarnall/bagpipes>.

<sup>5</sup>  $a_e^{(\text{gal})}$  is the semi-major axis of the ellipse which encloses half of the total light of the galfit model of the galaxy.



the galfit F814W magnitude  $m_{\text{F814W}}^{(\text{gal})}$  by the circularized effective area (Eq. 4, Dressler et al. 1987), and then converting it through Eq. (5) to  $I_e$ , which is expressed in units of solar luminosity  $L_\odot$  per square parsec (4.52 is the absolute AB magnitude of the Sun in the HST F814W band, as reported in Table 3 of Willmer 2018):

$$\mu_e = m_{\text{F814W}}^{(\text{gal})} + 2.5 \log(2\pi) + 5 \log\left(\frac{R_e}{1''}\right) \quad (4)$$

$$\log(I_e) = -0.4 [\mu_e - 21.572 - 10 \log(1 + z_c) - 4.52] \quad (5)$$

Following the prescriptions of Jørgensen et al. (1996), we computed  $\sigma_{e8}$  by correcting the LOSVD to an aperture of  $R_e/8$  using Eq. (6) and Eq. (7) from Zhu et al. (2023), where we used the value  $\kappa = -0.033$  measured by de Graaff et al. (2021):

$$\sigma_{e8} = \text{LOSVD} \cdot \left(\frac{R_e/8}{R_e}\right)^{\kappa_{\text{circ}}} \quad (6)$$

$$\kappa_{\text{circ}} = \kappa - 0.106(1 - q)^{4.73} \quad (7)$$

We used Itsfit<sup>6</sup> (Cappellari et al. 2009, 2013) to fit the FP of PLCK-G287 using  $\sigma_{e8}$  expressed in  $\text{km s}^{-1}$ ,  $I_e$  in  $L_\odot \text{ pc}^{-2}$ , and  $R_e$  in kpc. Following the Itsfit guidelines, we also increased the  $\sigma$ -clipping threshold from the default value of 2.6 standard deviations to 4 standard deviations to reduce the number of objects identified as outliers. The best-fitting plane, shown in Fig. 1, has coefficients  $\alpha = 1.2 \pm 0.1$  and  $\beta = -0.72 \pm 0.04$ , and a scatter of  $\Delta = 0.09$ . These values are consistent with those reported in the literature.

#### 4.1. The stellar mass and stellar mass fraction hyperplanes

By correlating the residuals of the best-fitting plane with the physical parameters inferred with Bagpipes (such as the metallicity, mass-weighted age,  $\tau$ ,  $T_0$ ,  $A_V$ , etc.), we found a clear trend only with the stellar mass (Fig. B.2). We therefore extended the FP by using  $\log(M^*)$  as a fourth dimension ( $M^*$ -HP, Eq. 8), with  $M^*$  expressed in units of  $M_\odot$ :

$$\log(R_e) = \alpha \log(\sigma_{e8}) + \beta \log(I_e) + \epsilon \log(M^*) + \gamma \quad (8)$$

As we did for the classic FP, we fitted this stellar mass hyperplane with Itsfit and the best-fit plane resulted in a very tight relation with a scatter of  $\Delta = 0.023$  (Fig. 2), with only two ETGs identified as  $4\sigma$  outliers. However, the coefficients  $\alpha = 0.24 \pm 0.08$ ,  $\beta = -0.62 \pm 0.02$ , and  $\epsilon = 0.46 \pm 0.03$  cannot be directly linked to those of the classic FP.

We then relaxed the hypothesis that  $f_e^*$  is constant across the ETGs sample, while assuming that the virial theorem still holds and that  $M_e^*/L_e$  is constant. In that case, the Eq. (2) can be written as Eq. ( $f_e^*$ -HP, 9), which describes a 4D stellar mass fraction hyperplane extension of the classical FP, where the coefficients  $\alpha$  and  $\beta$  theoretically are still 2 and  $-1$ , respectively, and  $\epsilon = 1$ :

$$\log(R_e) = \alpha \log(\sigma_{e8}) + \beta \log(I_e) + \epsilon \log(f_e^*) + \gamma \quad (9)$$

<sup>6</sup> Itsfit: a Python package for very robust hyperplane fitting in N dimensions. See: <https://pypi.org/project/itsfit>.

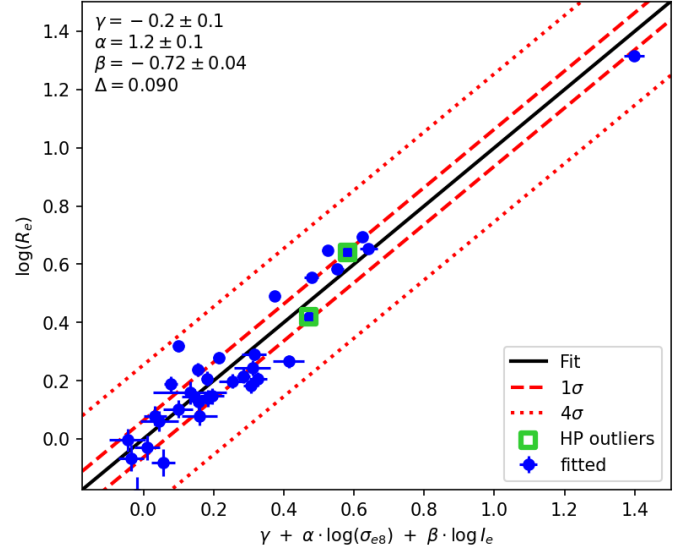


**Fig. 1.** Fit to the classic FP (Eq. 1) built with a sample of 35 secure ETGs selected as members of the galaxy cluster PLCK-G287, where the aperture-corrected central stellar velocity dispersion  $\sigma_{e8}$  is expressed in  $\text{km s}^{-1}$ , the surface brightness  $I_e$  in  $L_\odot \text{ pc}^{-2}$ , and the circularized effective radius  $R_e$  in kpc. The solid black line is the projection of the best-fitting plane, while the red dashed and dotted lines indicate the 1 and 4 standard deviation intervals, respectively. Green squares indicate the two objects that are found to be outliers of the  $M^*$  and  $f_e^*$  hyperplanes (see Sec. 4.1).

Observations show that the total mass distribution of ETGs, up to  $2R_e$ , is well describe by a singular isothermal sphere (SIS, see for example Mould et al. 1990 and Arnaboldi et al. 1998), whose density profile is:

$$\rho(r) = \frac{\sigma_{\text{SIS}}^2}{2\pi G r^2} \quad (10)$$

Since it has been tested that  $\sigma_{\text{SIS}} \simeq \sigma_{e8}$  (e.g. Treu et al. 2006; Bolton et al. 2008; Grillo et al. 2008), the projected total mass  $M_e$  enclosed in a cylinder of radius  $R_e$  can be derived from:

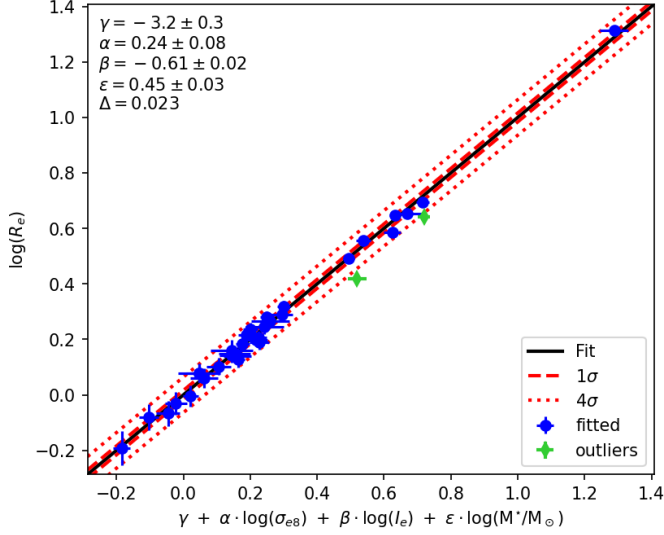
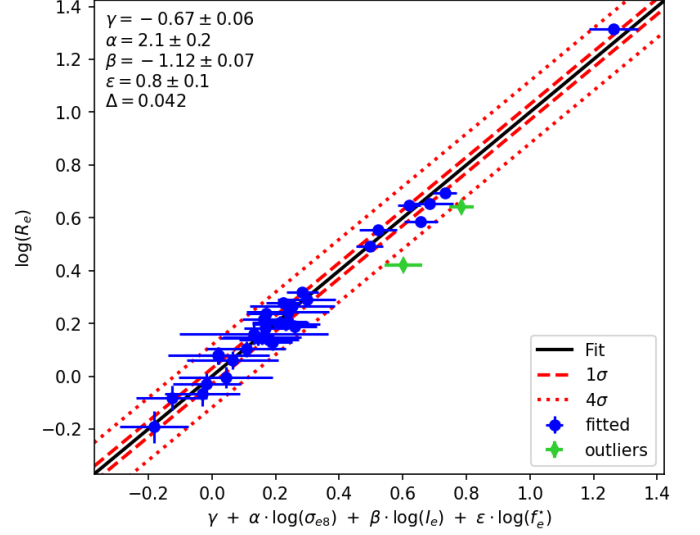
$$M_e = \frac{\pi}{G} \sigma_{e8}^2 R_e \quad (11)$$

and, therefore,  $f_e^* = 0.5M^*/M_e$  (see Fig. B.1). The Itsfit best-fitting plane has coefficients  $\alpha = 2.1 \pm 0.2$ ,  $\beta = -1.12 \pm 0.07$ , and  $\epsilon = 0.8 \pm 0.1$ , which are compatible with the theoretical ones (Fig. 3). The scatter  $\Delta = 0.042$  is higher than the value for the  $M^*$ -HP, however it is still less than half of the scatter of the FP. As in the previous case, only two galaxies are identified as  $4\sigma$  outliers.

Finally, for the FP and the two HPs, we also computed the Ezekiel adjusted coefficient of determination ( $\overline{R}^2$ , Raju et al. 1997), the Akaike information criterion (AIC, Akaike 2015), and the Bayesian information criterion (BIC, Schwarz 2007). Their values are summarized in table 1, along with the best fitting parameters. For both  $f_e^*$ -HP and  $M^*$ -HP, the higher values of  $\overline{R}^2$  together with the lower values of AIC and BIC with respect to those of the FP, indicate that the decrease of the scatter in these two HPs cannot be attributed to, for example, the increase of the dimensionality of the parameter space, but rather to the additional information brought in by the stellar mass values.

**Table 1.** Summary of the fundamental plane and hyper-planes equations with the corresponding best-fitting parameters and figure of merits.

	(Hyper-)plane equation	Best-fit parameters				Scatter $\Delta$	$\overline{R^2}$	AIC	BIC
		$\alpha$	$\beta$	$\epsilon$	$\gamma$				
FP	$\log(R_e) = \alpha \log(\sigma) + \beta \log(I_e) + \gamma$	$1.2 \pm 0.1$	$-0.72 \pm 0.04$		$-0.2 \pm 0.1$	0.090	0.903	$-6.5 \times 10^1$	$-6.2 \times 10^1$
$M^*$ -HP	$\log(R_e) = \alpha \log(\sigma_{e8}) + \beta \log(I_e) + \epsilon \log(M^*) + \gamma$	$0.24 \pm 0.08$	$-0.62 \pm 0.02$	$0.46 \pm 0.03$	$-3.2 \pm 0.3$	0.023	0.989	$-1.3 \times 10^2$	$-1.3 \times 10^2$
$f_e^*$ -HP	$\log(R_e) = \alpha \log(\sigma) + \beta \log(I_e) + \epsilon \log(f_e^*) + \gamma$	$2.1 \pm 0.2$	$-1.12 \pm 0.07$	$0.8 \pm 0.1$	$-0.67 \pm 0.06$	0.042	0.963	$-8.9 \times 10^1$	$-8.4 \times 10^1$

**Fig. 2.** Fit to the stellar mass hyperplane (Eq. 8) built with a sample of 35 secure ETG members of the galaxy cluster PLCK-G287, where the aperture-corrected central velocity dispersion  $\sigma_{e8}$  is expressed in  $\text{km s}^{-1}$ , the surface brightness  $I_e$  in  $L_\odot \text{pc}^{-2}$ , the stellar mass  $M^*$  in  $M_\odot$ , and the circularized effective radius  $R_e$  in kpc. The solid black line is the projection of the best-fitting plane, while the red dashed and dotted lines indicate the 1 and 4 standard deviation intervals, respectively. Green points are objects identified as outliers and therefore not included in the fit.**Fig. 3.** Fit to the stellar mass fraction hyperplane (Eq. 9) built with a sample of 35 secure ETG members of the galaxy cluster PLCK-G287, where the aperture-corrected central velocity dispersion  $\sigma_{e8}$  is expressed in  $\text{km s}^{-1}$ , the surface brightness  $I_e$  in  $L_\odot \text{pc}^{-2}$ , and the circularized effective radius  $R_e$  in kpc. The solid black line is the projection of the best-fitting plane, while the red dashed and dotted lines indicate the 1 and 4 standard deviation intervals, respectively. Green points are objects identified as outliers and therefore not included in the fit.

## 5. Discussion

In our sample of ETGs, we do not observe any evident trend in  $M_e^*/L_e$  with respect to  $\log(\sigma_{e8})$  and  $\log(L_e)$  (see Fig. B.4), while there appears to be only a weak trend with respect to  $\log(R_e)$ . This, together with the fact that the coefficients  $\alpha = 2.1 \pm 0.2$ ,  $\beta = -1.12 \pm 0.07$  of the  $f_e^*$ -HP are consistent with the theoretical values derived by the virial theorem, indicates that the selection criteria we adopted can be used to build a quite pure sample of virialized ETG and it corroborates the idea that the major contribution to the tilt of the FP comes from variations in the dark matter content, as highlighted for example in de Graaff et al. (2022), instead of stellar population effects, like suggested for example in Grillo & Gobat (2010). The value of the scatter in the  $f_e^*$ -HP is 50% lower than one the classic FP, which confirms what has been observed, for example, by Dogruel et al. (2024), who found a decrease of the scatter of  $\sim 10\%$  when extending the FP to a hyperplane. Our sample of galaxies has a mean  $f_e^* \approx 35\%$ , which corresponds to an average fraction of dark matter within  $R_e$  of approximately  $f_e^{DM} \approx 65\%$ . Since  $f_e^*$  is computed using the projected total mass within a cylinder of radius  $R_e$ , this value cannot be directly compared to those from other studies that estimate the total masses using a three-dimensional dynamical model (e.g.: Gerhard et al. 2001; Cappellari et al. 2006; Tortora et al. 2009;

Thomas et al. 2007, 2011), however, it is consistent with the average dark matter fraction value of  $\sim 60\%$  measured by Grillo (2010) using two-dimensional total masses.

Projecting the  $f_e^*$ -HP in lower dimensional spaces, for example by making an orthogonal projection along the  $f_e^*$  axis, highlights how ETGs with different  $f_e^*$  lie on FPs with different slopes and intercepts (See Fig. B.3). Therefore, we can interpret the FP not as a plane in the strict sense, but as a surface that originates from a non-edge-on projection of a higher-dimensional hyperplane, which is in line with the findings of Yoon & Park (2022).

The coefficient  $\epsilon = 0.8 \pm 0.1$  of the  $f_e^*$ -HP is also compatible with the theoretical value of 1 within  $2\sigma$ , even if it is not perfectly on point. This could indicate the presence of measurement errors caused, for example, by  $M^*/L$  gradients, which can bias the estimate of the effective radius (Bernardi et al. 2023). Since we already used  $M^*$  to estimate the stellar mass fraction  $f_e^*$ , only an independent estimation of  $M^*/L$  would reveal the nature of this remaining small tilt. In future works, it could be worth also studying how this coefficient varies by using other mass profiles more complex than the SIS (even at the expense of an increasing number of free parameters).

The  $M^*$ -HP has a scatter that is half that of the  $f_e^*$ -HP, even if the coefficients cannot be linked immediately to any physical-law derivation, like the ones of the  $f_e^*$ -HP. However, this is probably why the scatter is so small, since there is no assumption about the shape of the total mass profile or about the  $M_e^*/L_e$  and  $f_e^*$  being constant. Moreover, the  $M^*$  estimates are actually independent of the other three parameters of the hyperplane. The variations of  $M_e^*/L_e$  across this sample of ETGs, instead, could account for the remaining scatter in the  $M^*$ -HP. On the other hand, the fact that the scatter in the  $M^*$ -HP is lower than in the  $f_e^*$ -HP seems to support the idea that the tilt and the scatter, despite being strictly linked one to another, do not have the same origin. The stellar mass we derived from stellar population analysis, in fact, could be thought to bring also information about the properties of stellar population, such as the age, the metallicity, etc., that can contribute significantly to the scatter (as shown for example in [Gargiulo et al. 2009](#)). In future works, when considering a large sample of galaxies and at different redshifts, it will be interesting to determine to what extent the scatter can be further reduced by extending the  $M^*$ -HP and  $f_e^*$ -HP with other stellar population parameters.

*Acknowledgements.* This work is based on observations taken by the RELICS Treasury Program (GO 14096) with the NASA/ESA HST, which is operated by the Association of Universities for Research in Astronomy, Inc., under NASA contract NAS5-26555. Based on observations collected at the European Southern Observatory under ESO programme(s) 0102.A-0640(A) and/or data obtained from the ESO Science Archive Facility with DOI(s) under <https://doi.org/10.18727/archive/41>. We acknowledge financial support through grant PRIN-MIUR 2020SKSTHZ. AM acknowledges financial support through grant NextGenerationEU" RFF M4C2 1.1 PRIN 2022 project 2022ZSL4BL IN-SIGHT.

## References

- Akaike, H. 2015, Information Theory and an Extension of the Maximum Likelihood Principle
- Arnaboldi, M., Freeman, K. C., Gerhard, O., et al. 1998, *The Astrophysical Journal*, 507, 759
- Arsenault, R., Madec, P.-Y., Hubin, N., et al. 2008, in *Adaptive Optics Systems*, Vol. 7015
- Bacon, R., Copin, Y., Monnet, G., et al. 2001, *Monthly Notices of the Royal Astronomical Society*, 326
- Bagchi, J., Sirothia, S. K., Werner, N., et al. 2011, *The Astrophysical Journal*, 736, L8
- Bender, R., Burstein, D., & Faber, S. M. 1992, *The Astrophysical Journal*, 399, 462
- Bergamini, P., Rosati, P., Mercurio, A., et al. 2019, *Astronomy and Astrophysics*, 631
- Bernardi, M., Domínguez Sánchez, H., Margalef-Bentabol, B., Nikakhtar, F., & Sheth, R. K. 2020, *Monthly Notices of the Royal Astronomical Society*, 494, 5148
- Bernardi, M., Sánchez, H. D., Sheth, R. K., Brownstein, J. R., & Lane, R. R. 2022, *Monthly Notices of the Royal Astronomical Society*, 518, 4713
- Bernardi, M., Sheth, R. K., Annis, J., et al. 2003, *The Astronomical Journal*, 125, 1866
- Bernardi, M., Sheth, R. K., Domínguez-Sánchez, H., et al. 2018, *Monthly Notices of the Royal Astronomical Society*, 477, 2560
- Bernardi, M., Sheth, R. K., Domínguez Sánchez, H., et al. 2023, *Monthly Notices of the Royal Astronomical Society*, 518
- Bertini, E. 1996, *Astronomy and Astrophysics Supplement Series*, 117
- Bezanson, R., van Dokkum, P. G., van de Sande, J., et al. 2013, *The Astrophysical Journal*, 779, L21
- Birrer, S., Shajib, A. J., Galan, A., et al. 2020, *Astronomy & Astrophysics*, 643, A165
- Bolton, A. S., Burles, S., Koopmans, L. V. E., et al. 2008, *The Astrophysical Journal*, 682
- Bonafede, A., Intema, H. T., Brüggén, M., et al. 2014, *The Astrophysical Journal*, 785, 1
- Bundy, K., Bershady, M. A., Law, D. R., et al. 2015, Overview of the SDSS-IV MaNGA survey: Mapping Nearby Galaxies at Apache Point Observatory
- Busarello, G., Capaccioli, M., Capozziello, S., Longo, G., & Puddu, E. 1997, *Astronomy and Astrophysics*, 320
- Calzetti, D. 2001, *The Publications of the Astronomical Society of the Pacific*, Volume 113, Issue 790, pp. 1449-1485., 113, 1449
- Calzetti, D., Armus, L., Bohlin, R. C., et al. 2000, *The Astrophysical Journal*, 533
- Caminha, G. B., Rosati, P., Grillo, C., et al. 2019, *Astronomy and Astrophysics*, 632
- Cappellari, M. 2017, *Monthly Notices of the Royal Astronomical Society*, 466
- Cappellari, M. 2023, *Monthly Notices of the Royal Astronomical Society*, 526
- Cappellari, M., Bacon, R., Bureau, M., et al. 2006, *Monthly Notices of the Royal Astronomical Society*, 366
- Cappellari, M. & Emsellem, E. 2004, *Publications of the Astronomical Society of the Pacific*, 116
- Cappellari, M., Emsellem, E., Bacon, R., et al. 2007, *Monthly Notices of the Royal Astronomical Society*, 379
- Cappellari, M., Emsellem, E., Krajnović, D., et al. 2011, *Monthly Notices of the Royal Astronomical Society*, 413, 813
- Cappellari, M., Scott, N., Alatalo, K., et al. 2013, *Monthly Notices of the Royal Astronomical Society*, 432, 1709
- Cappellari, M., Scott, N., Alatalo, K., et al. 2009, *Proceedings of the International Astronomical Union*, 5, 81
- Carnall, A. C., Leja, J., Johnson, B. D., et al. 2019a, *The Astrophysical Journal*, 873, 44
- Carnall, A. C., McLure, R. J., Dunlop, J. S., et al. 2019b, *Monthly Notices of the Royal Astronomical Society*, 490
- Carnall, A. C., McLure, R. J., Dunlop, J. S., & Davé, R. 2018, *Monthly Notices of the Royal Astronomical Society*, 480
- Coe, D., Salmon, B., Bradač, M., et al. 2019, *The Astrophysical Journal*, 884
- Croom, S. M., Lawrence, J. S., Bland-Hawthorn, J., et al. 2012, *Monthly Notices of the Royal Astronomical Society*, 421, no
- D'Addona, M., Mercurio, A., Rosati, P., et al. 2024, *Astronomy & Astrophysics*
- de Graaff, A., Bezanson, R., Franx, M., et al. 2021, *The Astrophysical Journal*, 913, 103
- de Graaff, A., Franx, M., Bell, E. F., et al. 2022, *Monthly Notices of the Royal Astronomical Society*, 518, 5376
- Djorgovski, S. & Davis, M. 1987, *The Astrophysical Journal*, 313
- Dogrueel, M. B., Taylor, E. N., Cluver, M., et al. 2024, *The Astrophysical Journal*, 970, 149
- Dogrueel, M. B., Taylor, E. N., Cluver, M., et al. 2023, *The Astrophysical Journal*, 953, 45
- Dressler, A., Lynden-Bell, D., Burstein, D., et al. 1987, *The Astrophysical Journal*, 313, 42
- D'Eugenio, F., Colless, M., Scott, N., et al. 2021, *Monthly Notices of the Royal Astronomical Society*, 504, 5098
- D'Eugenio, F., Colless, M., van der Wel, A., et al. 2024, *Monthly Notices of the Royal Astronomical Society*, 532, 1775
- D'Onofrio, M., Cariddi, S., Chiosi, C., Chiosi, E., & Marziani, P. 2017, *The Astrophysical Journal*, 838, 163
- D'Onofrio, M. & Chiosi, C. 2024, *Astronomy & Astrophysics*, 687, A126
- Faber, S. M. 1987, *Astronomische Nachrichten*, 310
- Faber, S. M. & Jackson, R. E. 1976, *The Astrophysical Journal*, 204
- Fernández Lorenzo, M., Cepa, J., Bongiovanni, A., et al. 2011, *Astronomy and Astrophysics*, 526
- Feroz, F. & Hobson, M. P. 2008, *Monthly Notices of the Royal Astronomical Society*, 384
- Feroz, F., Hobson, M. P., & Bridges, M. 2009, *Monthly Notices of the Royal Astronomical Society*, 398
- Feroz, F., Hobson, M. P., Cameron, E., & Pettitt, A. N. 2019, *The Open Journal of Astrophysics*, 2
- Ferrero, I., Navarro, J. F., Abadi, M. G., Benavides, J. A., & Mast, D. 2021, *Astronomy & Astrophysics*, 648, A124
- Finner, K., Jee, M. J., Golovich, N., et al. 2017, *The Astrophysical Journal*, 851
- Gargiulo, A., Haines, C. P., Merluzzi, P., et al. 2009, *Monthly Notices of the Royal Astronomical Society*, 397, 75
- Gerhard, O., Kronawitter, A., Saglia, R. P., & Bender, R. 2001, *The Astronomical Journal*, 121
- Granata, G., Mercurio, A., Grillo, C., et al. 2022, *Astronomy and Astrophysics*, 659
- Grèbol-Tomàs, P., Ferré-Mateu, A., & Domínguez-Sánchez, H. 2023, *Monthly Notices of the Royal Astronomical Society*, 526
- Grillo, C. 2010, *The Astrophysical Journal*, 722, 779
- Grillo, C. & Gobat, R. 2010, *Monthly Notices of the Royal Astronomical Society: Letters*, 402, L67
- Grillo, C., Lombardi, M., & Bertin, G. 2008, *Astronomy & Astrophysics*, 477, 397
- Grillo, C., Suyu, S. H., Rosati, P., et al. 2015, *The Astrophysical Journal*, 800, 38
- Gruen, D., Seitz, S., Brimiouille, F., et al. 2014, *Monthly Notices of the Royal Astronomical Society*, 442, 1507
- Hyde, J. B. & Bernardi, M. 2009a, *Monthly Notices of the Royal Astronomical Society*, 394
- Hyde, J. B. & Bernardi, M. 2009b, *Monthly Notices of the Royal Astronomical Society*, 396, 1171
- Jørgensen, I., Chiboucas, K., Flint, K., et al. 2006, *The Astrophysical Journal*, 639
- Jørgensen, I., Franx, M., & Kjaergaard, P. 1996, *Monthly Notices of the Royal Astronomical Society*, 280
- Khanday, S. A., Saha, K., Iqbal, N., Dhiwar, S., & Pahwa, I. 2022, *Monthly Notices of the Royal Astronomical Society*, 515, 5043
- Kluge, M. & Bender, R. 2023, *The Astrophysical Journal Supplement Series*, 267
- Kollmeier, J., Anderson, S. F., Blanc, G. A., et al. 2019, *BAAS*, 51, 274
- Kormendy, J. 1977a, *The Astrophysical Journal*, 214
- Kormendy, J. 1977b, *The Astrophysical Journal*, 218
- Kormendy, J. 1977c, *The Astrophysical Journal*, 217
- Kormendy, J. 1985, *The Astrophysical Journal*, 295
- Kroupa, P. & Boily, C. M. 2002, *Monthly Notices of the Royal Astronomical Society*, 336, 1188
- Li, H., Mao, S., Cappellari, M., et al. 2018, *Monthly Notices of the Royal Astronomical Society*, 476, 1765
- Marsden, C., Shankar, F., Bernardi, M., et al. 2022, *Monthly Notices of the Royal Astronomical Society*, 510
- Mercurio, A., Merluzzi, P., Haines, C. P., et al. 2006, *Monthly Notices of the Royal Astronomical Society*, 368
- Monna, A., Seitz, S., Zitrin, A., et al. 2015, *Monthly Notices of the Royal Astronomical Society*, 447
- Mould, J. R., Oke, J. B., de Zeeuw, P. T., & Nemec, J. M. 1990, *The Astronomical Journal*, 99, 1823
- Pahre, M. A., Djorgovski, S. G., & de Carvalho, R. R. 1998, *The Astronomical Journal*, 116
- Peng, C. Y., Ho, L. C., Impey, C. D., & Rix, H.-W. 2002, *The Astronomical Journal*, 124
- Peng, C. Y., Ho, L. C., Impey, C. D., & Rix, H.-W. 2010, *The Astronomical Journal*, 139, 2097
- Prugniel, P., Simien, F., Prugniel, P., & Simien, F. 1994, *A&A*, 282, L1
- Raju, N. S., Bilgic, R., Edwards, J. E., & Fleer, P. F. 1997, *Methodology review: Estimation of population validity and cross-validity, and the use of equal weights in prediction*
- Rosito, M. S., Pedrosa, S. E., Tissera, P. B., et al. 2021, *Astronomy and Astrophysics*, 652

- Saglia, R. P., Bender, R., & Dressler, A. 1993, 279, 75
- Schwarz, G. 2007, The Annals of Statistics, 6
- Seitz, S. 2016, Revealing the largest gravitational lens PLCK G287.0+32.9
- Straatman, C. M. S., Wel, A. v. d., Bezanson, R., et al. 2018, The Astrophysical Journal Supplement Series, 239, 27
- Ströbele, S., La Penna, P., Arsenault, R., et al. 2012, in Adaptive Optics Systems III, Vol. 8447
- Thomas, J., Saglia, R. P., Bender, R., et al. 2007, Monthly Notices of the Royal Astronomical Society, 382
- Thomas, J., Saglia, R. P., Bender, R., et al. 2011, Erratum: Dynamical masses of early-type galaxies: A comparison to lensing results and implications for the stellar initial mass function and the distribution of dark matter
- Tortora, C., Napolitano, N. R., Romanowsky, A. J., Capaccioli, M., & Covone, G. 2009, Monthly Notices of the Royal Astronomical Society, 396, 1132
- Tortorelli, L. & Mercurio, A. 2023, Frontiers in Astronomy and Space Sciences, 10
- Tortorelli, L., Mercurio, A., Granata, G., et al. 2023, Astronomy and Astrophysics, 671
- Tortorelli, L., Mercurio, A., Paolillo, M., et al. 2018, Monthly Notices of the Royal Astronomical Society, 477
- Treu, T., Koopmans, L. V., Bolton, A. S., Burles, S., & Moustakas, L. A. 2006, The Astrophysical Journal, 640
- van de Sande, J., Kriek, M., Franx, M., Bezanson, R., & van Dokkum, P. G. 2014, The Astrophysical Journal, 793, L31
- van der Wel, A., Noeske, K., Bezanson, R., et al. 2016, The Astrophysical Journal Supplement Series, 223, 29
- Weilbacher, P. M., Palsa, R., Streicher, O., et al. 2020, Astronomy and Astrophysics, 641
- Weiner, B. J., Willmer, C. N. A., Faber, S. M., et al. 2006, The Astrophysical Journal, 653
- Westfall, K. B., Cappellari, M., Bershady, M. A., et al. 2019, The Astronomical Journal, 158
- Willmer, C. N. A. 2018, The Astrophysical Journal Supplement Series, 236, 47
- Yoon, Y. & Park, C. 2020, The Astrophysical Journal, 897, 121
- Yoon, Y. & Park, C. 2022, The Astrophysical Journal, 936, 22
- Zhu, K., Li, R., Cao, X., et al. 2023, Research in Astronomy and Astrophysics, 23, 085001
- Zhu, K., Lu, S., Cappellari, M., et al. 2024, Monthly Notices of the Royal Astronomical Society, 527
- Zitrin, A., Seitz, S., Monna, A., et al. 2017, The Astrophysical Journal, 839, L11



## Appendix A: Tables

**Table A.1.** Parameters of the secure ETG sample.

ID	R.A. [ICRS]	Dec. [ICRS]	$m_{\text{F814W}}^{(\text{gal})}$ [mag.]	$n$	$q$	$a_e^{(\text{gal})}$ [ $''$ ]	LOSVD [km s $^{-1}$ ]	$M^*$ [ $10^{10} \text{ M}_\odot$ ]	$f_e^*$	...
266	177.723504	−28.097371	18.335	4.10	0.71	1.01	285	7.2	0.238	...
344	177.716485	−28.099784	19.123	3.82	0.79	0.82	232	4.31	0.248	...
366	177.720875	−28.098379	19.238	3.16	0.95	0.61	198	3.71	0.355	...
430	177.728033	−28.095713	19.747	4.21	0.79	0.56	221	3.33	0.300	...
⋮	⋮	⋮	⋮	⋮	⋮	⋮	⋮	⋮	⋮	⋮

**Notes.** This is an extract of the full table, which is only available in electronic form at the CDS. The first column (ID) contains the ID of the objects from the spectroscopic catalog published in [D24](#); the second and third columns show the J2000 ICRS right ascension and declination (R.A and Dec.); the fourth one ( $m_{\text{F814W}}^{(\text{gal})}$ ) contains the magnitude from the Galfit best-fit made in HST band F814W (see. ); the fifth column ( $n$ ) reports the Sérsic index; the sixth one ( $q$ ) contains the axis ratio; the seventh one ( $a_e^{(\text{gal})}$ ) contains the Galfit effective semi-major axis in arcseconds; the eighth column reports the LOSVD in km s $^{-1}$ ; the ninth one ( $M^*$ ) contains the total stellar mass in units of  $10^{10} \text{ M}_\odot$ ; the tenth one ( $f_e^*$ ) contains the stellar over total mass fraction, namely, the ratio between the stellar mass and the total mass within a circle of radius  $R_e$ . Columns eleven to seventeen, not reported here, contain the errors for the values in columns four to ten, respectively.

## Appendix B: Additional figures

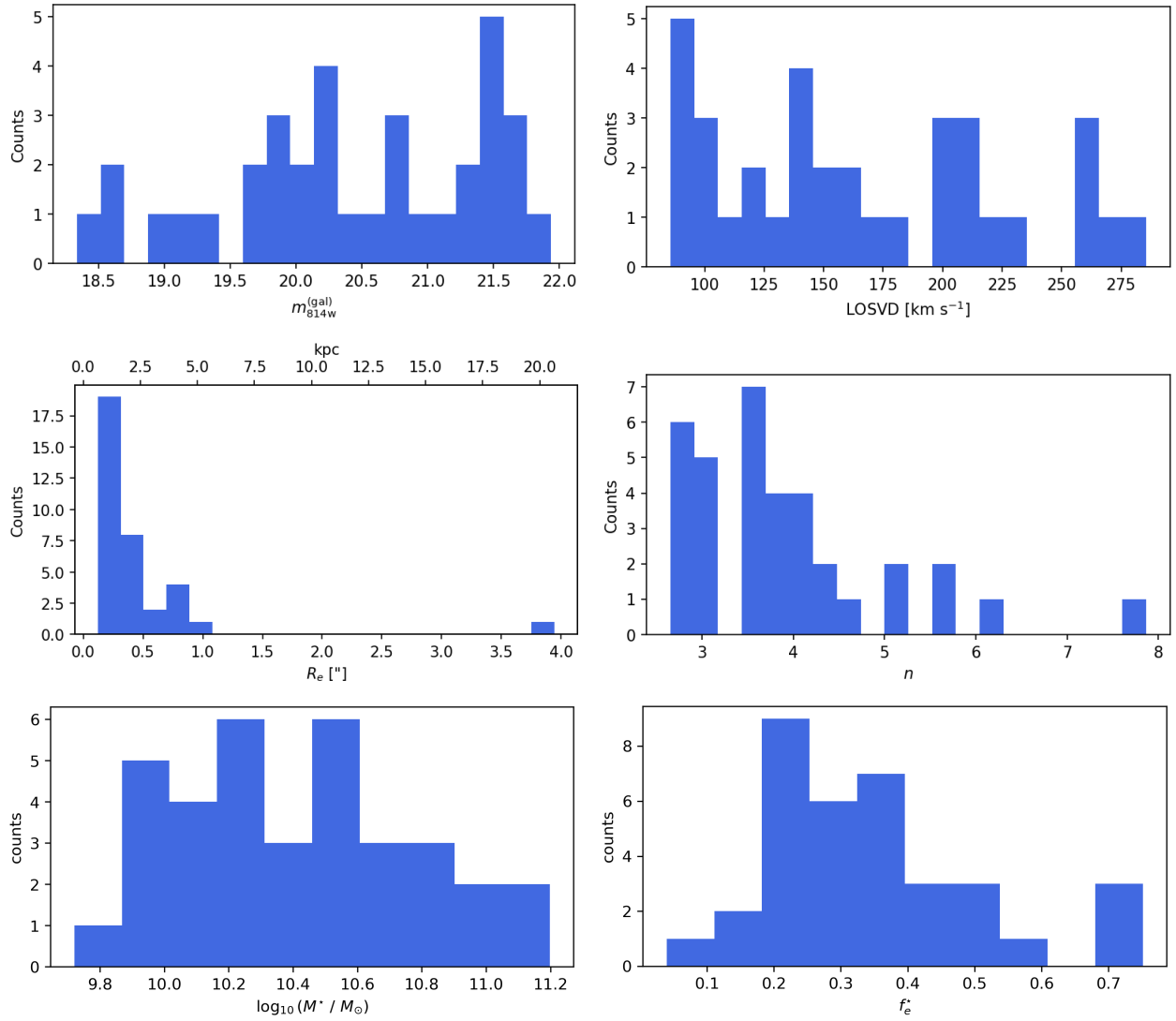


**Fig. B.1.** Distribution of the ETGs used to fit the FP as a function of the galfit magnitude in HST band F814W (top-left panel), the LOSVD (top-right panel), the circularized effective radius (middle-left panel), the Sérsic index (middle-right panel), the stellar mass (bottom-left panel) and stellar over total mass fraction  $f_e^*$  (bottom-right panel).

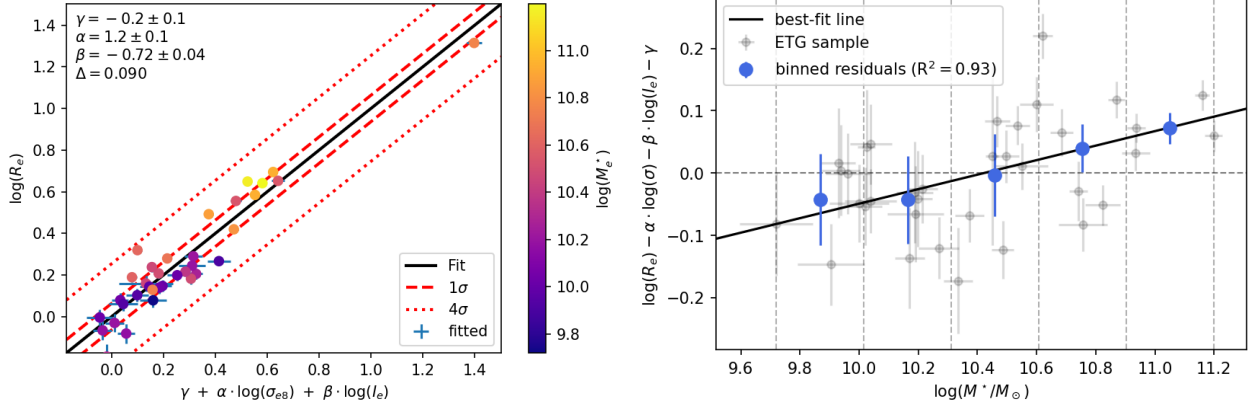


**Fig. B.2.** Classic FP of PLCK-G287 with points colored as a function of the stellar mass (left panel) and residuals of the classic FP as a function of  $M^*$  (right panel). Gray points are the ETGs used to fit the FP. A linear fit (solid black line) shows a clear relation between  $M^*$  and the residuals. As a reference, we also show the average residuals (blue points) computed in five bins of equal width of the stellar mass, which are indicated by the vertical dashed gray lines. The value of correlation coefficient  $R^2 = 0.93$  computed using these binned residuals confirms the linear relation with the stellar mass.

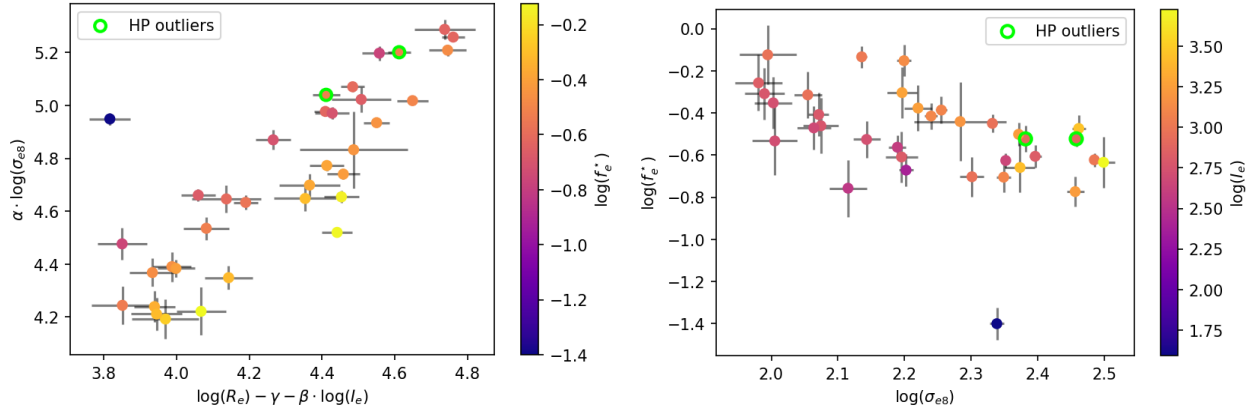


**Fig. B.3.** Two projections of the stellar mass fraction hyperplane: one with  $\log(\sigma_{88})$  as a function of  $\log(R_e) - \gamma - \beta \log(l_e)$  (left panel) and one with  $\log(f_e^*)$  as a function of  $\log(\sigma_{88})$  (right panel). The color of the points indicates the value of  $\log(f_e^*)$  and to  $\log(l_e)$ , respectively. Both plots highlight the dependency on the stellar mass fraction. The one on the left, in particular, is another way to plot the FP and shows how ETGs with similar stellar mass fractions seem to lie on planes with different slopes and intercepts. The isolated object with a peculiarly low value of  $f_e^*$  is the one with  $n = 7.86$  described in appendix C.

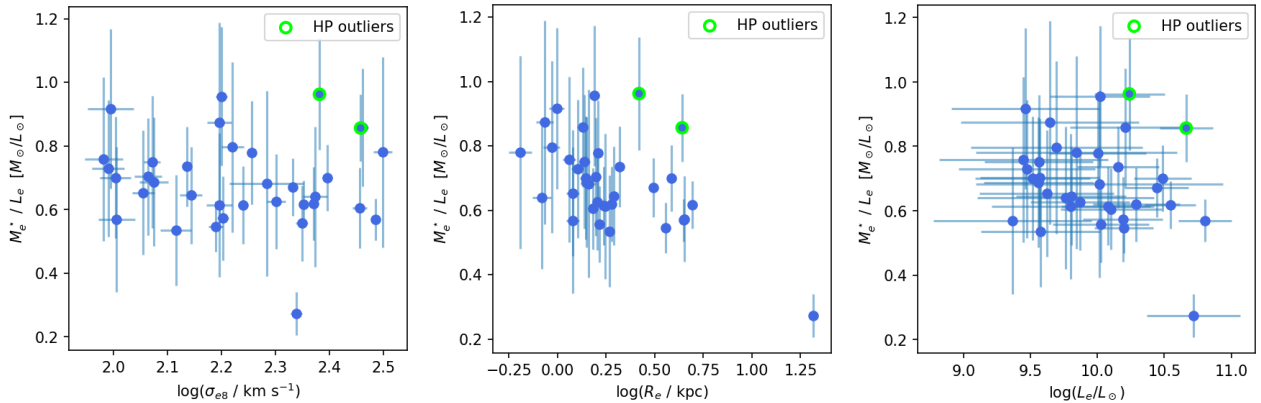


**Fig. B.4.** Stellar  $M/L$  ratio, computed within the circularized effective radius  $R_e$ , as a function of  $\log(\sigma_{88})$  (left panel),  $\log(R_e)$  (middle panel), and  $\log(L_e)$  (right panel). There is no evident trend in  $M_e^*/L_e$  with respect to  $\log(\sigma_{88})$  and  $\log(L_e)$ . There seems to be also a weak trend with respect to  $\log(R_e)$  up to  $\sim 5.5$  kpc. The variations of  $M_e^*/L_e$  across this sample of galaxies could explain the remaining scatter in the stellar mass hyperplane.

### Appendix C: Robustness of hyperplane fitting

Initially, our sample of ETGs contained 38 galaxies, four of which showed a suspiciously large value of the Sérsic index. For this reason, we re-inspected the residuals of the Morphofit models and found that three of them actually showed faint substructures (see Fig. C.1, upper panel). Therefore, these three objects were then excluded from the sample, according to the selection criteria we illustrated in Sec. 3. The fourth one (ID=1129), with  $n = 7.86$ , has been kept in the sample as it did not present any sign of substructures, or an evident issue in the Morphofit model (C.1, lower panel). Interestingly, the value of the coefficients of the FP and the two HPs did not change significantly when the fit was performed using the sample of ETGs containing these three objects. This suggests that the fitting procedure is quite robust against the presence of spurious objects that do not strictly follow our selection criteria.

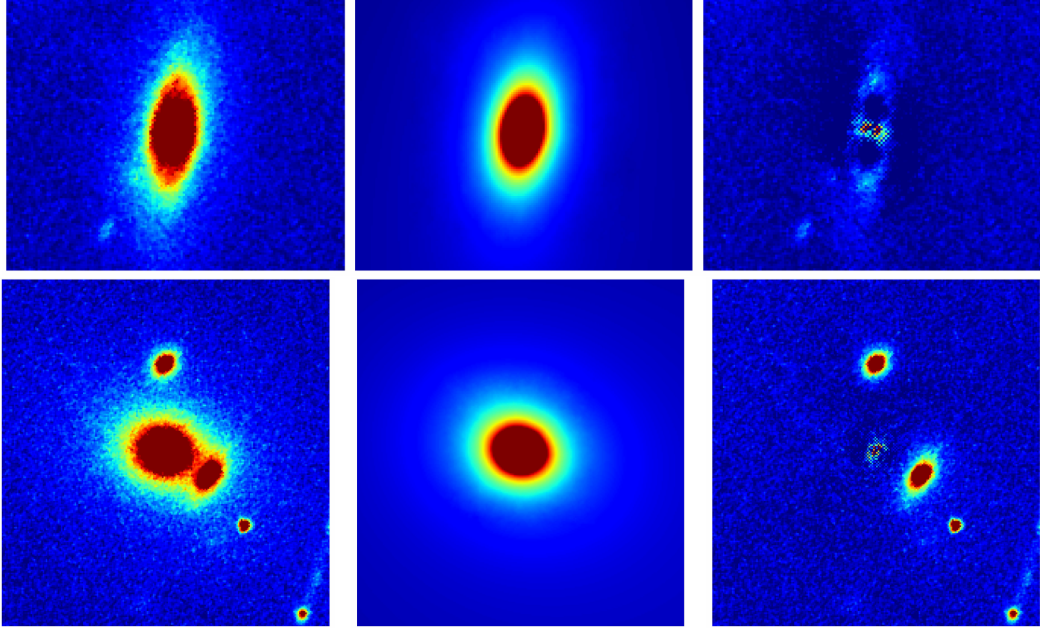


**Fig. C.1.** The upper panel shows one of the three galaxies that were removed from the original sample, due to the presence of substructures in the residuals of the Morphofit model. The lower panel shows the galaxy with  $n = 7.86$  that has been kept in the sample. From the left to the right, the columns show a cutout of the object taken from the HST F814W image, the corresponding Morphofit model, and the residual image.

The fourth object with ID=1129, due to its particularly large  $R_e$ , lies on the top right corner of the FP and HP plots. One could argue that, since it is relatively far from the other galaxies in the parameter space, it could have a large influence on the slope of the best fitting planes. So, to check whether this is the case, we performed the fit excluding this object and found that also in this case, the value of the coefficients of the two HPs are consistent with ones we previously found (see Fig. C.2). This not only corroborates the robustness of the fitting procedure, but it also confirms that this object follows the FP/HP scaling relations.

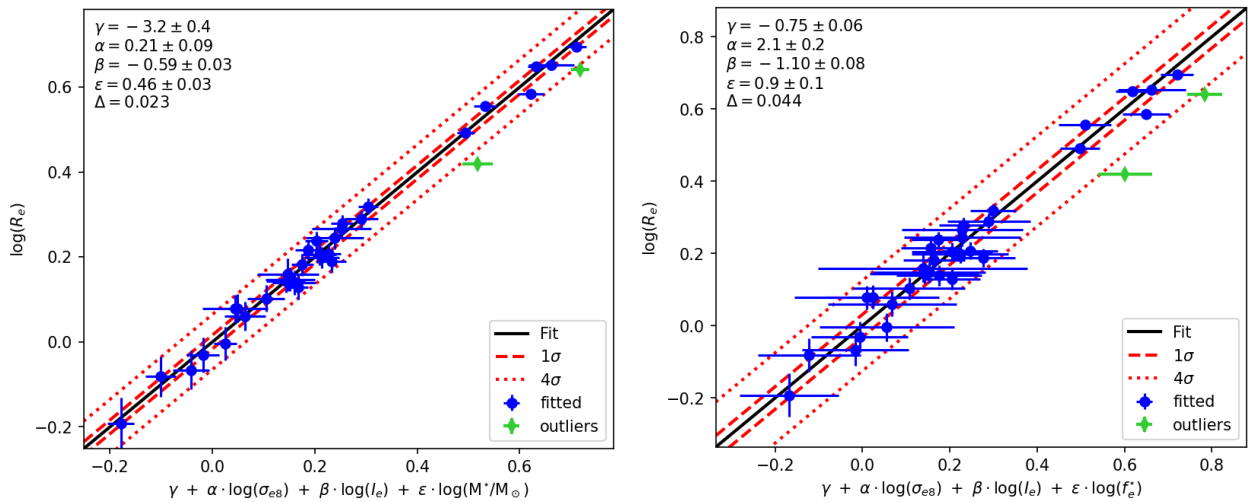


**Fig. C.2.** Fit to the stellar mass and mass fraction hyperplanes performed excluding the object with  $n = 7.86$ . The solid black line is the projection of the best-fitting plane, while the red dashed and dotted lines indicate the 1 and 4 standard deviation intervals, respectively. Green points are objects identified as outliers and therefore not included in the fit.